2017-05-01

Tidally induced residual current over the Malin Sea continental slope

stashchuk, N

http://hdl.handle.net/10026.1/8713

10.1016/j.csr.2017.03.010
Continental Shelf Research
Elsevier BV

Tidally induced residual current over the Malin Sea continental slope

Nataliya Stashchuk[a], Vasiliy Vlasenko[a], Phil Hosegood[a], W. Alex M. Nimmo-Smith[a],

[a]*School of Biological and Marine Sciences, University of Plymouth, Drake Circus, Plymouth, PL4 8AA, UK*

Abstract

Tidally induced residual currents generated over shelf-slope topography are investigated analytically and numerically using the Massachusetts Institute of Technology general circulation model. Observational support for the presence of such a slope current was recorded over the Malin Sea continental slope during 88-th cruise of the RRS "James Cook" in July 2013. A simple analytical formula developed here in the framework of time-averaged shallow water equations has been validated against a fully nonlinear non-hydrostatic numerical solution. A good agreement between analytical and numerical solutions is found for a wide range of input parameters of the tidal flow and bottom topography. In application to the Malin Shelf area both the numerical model and analytical solution predicted a northward moving current confined to the slope with its core located above the 400 m isobath and with vertically averaged maximum velocities up to 8 cm s^{-1}, which is consistent with the in-situ data recorded at three moorings and along cross-slope transects.

Keywords: Tides, slope currents, Malin shelf

1. Introduction

Warm and saline North Atlantic Waters moving northward along the European coast are an important element of the global meridional overturning circulation (White and Bowyer, 1997; Pingree and Le Cann, 1989; Huthnance and Gould, 1989). According to Huthnance (1995), Pingree and Le Cann (1989), this slope current is nearly barotropic. It is confined to the continental slope with its core typically located above the 500 m isobath and with maximum velocities ranging from 3 to 30 $\mathrm{cm\,s^{-1}}$. It was suggested by Huthnance (1984, 1986) and Hill et al. (1998) that the relatively steady character of this current reflects a density driven origin. The generation mechanism is associated with less-dense lower-latitude waters “standing high” compared to the northern basin. Note, however, that some other driving forces, e.g. wind, tides, horizontal pressure gradients can also contribute to the formation of the slope current (Huthnance et al., 2009).

The first systematic numerical studies of the slope current in the Malin Sea shelf/slope area were undertaken by Pingree and Le Cann (1989) who used a model domain with 10 km horizontal resolution for the region 40-64°N x 13-23°W. Vertically integrated model equations were used in a spherical polar coordinate system with a meridional variable Coriolis parameter. The model was forced by the M_2 tidal harmonic and a 10 $\mathrm{m\,s^{-1}}$ steady south-west wind blowing over 16 days. It was found that with such model settings the combination of tides and wind produces quite a weak residual slope current. Only the activation of horizontal buoyancy forcing which took into account the meridional density gradient allowed the generation of a slope current with velocity varying between 0.05 $\mathrm{m\,s^{-1}}$ on the Celtic Sea slope to 0.15 $\mathrm{m\,s^{-1}}$ off the Hebrides Island slope.

The most recent field experiments with Lagrangian drifters in the area (Charria et al., 2013; Porter et al., 2016) have shown that the structure of the slope current has seasonal periodicity. In the Bay of Biscay over the observational period from 2004 to 2009, the slope current was persistently directed poleward during the autumn-winter season (from October to March), but transported water in the opposite direction during the rest of the year Charria et al. (2013). In contrast, the drifter experiments conducted by Burrows and Thorpe (2002) above 55°N latitude showed the slope current to be strongly directed poleward during the whole year.

It is commonly believed that tides do not contribute greatly to the net water transport (Huthnance et al., 2009). Exception can be made for nonlinear effects when strong tidal motions generate internal solitary waves, as in the Celtic Sea, where these waves can transport water at the level of $O(1\,\mathrm{m}^2\,\mathrm{s}^{-1})$. This result is based on the theory by Huthnance (1986) who concluded that tidally driven slope currents account for only a small fraction of the slope currents usually observed. With respect to the Malin Sea shelf-slope area the principal baroclinic tidal effects recorded here were tidally generated internal solitary waves and bottom trapped internal Kelvin waves (see, for instance, Stashchuk and Vlasenko (2005, 2016) and references therein). However, as shown by Xing and Davies (2001) in a series of numerical experiments, nonlinear tidal effects at the Hebrides shelf edge can be responsible for the generation of an along slope current with velocities of up to $5\,\mathrm{cm\,s}^{-1}$.

In this paper we show that the role of tides in the formation of the slope currents in the Malin Sea shelf/slope area has been underestimated. Results of the numerical experiments conducted using the Massachusetts Institute of Technology general circulation model, MITgcm, (Marshall et al., 1997) reported here suggest tides to have a much greater role in the production of the along-slope transport than previously thought.

The paper is organised as follows. All historical observational data available for the area are discussed in Section 2. Section 3 describes high-resolution numerical experiments conducted for the Malin Shelf/Slope area. Section 4 presents an analytical solution for tidally rectified flows and numerical analysis that can prove this solution. Generalisation of the developed theory to the Malin Sea slope and its comparison with the MITgcm output are given in section 6. The paper finishes with a Discussion and Conclusions section.

2. Observational data

The observational data on the characteristics of the slope current over the Hebridean Slope are available from several field experiments. Measurements of White and Bowyer (1997) were conducted at two locations to the north-west of Ireland between 54.5°N and 55°N in April-December 1994. A persistent poleward along-slope current was recorded at both cross-sections with peak values up to $0.5\,\mathrm{m\,s^{-1}}$ at the position of steepest slope.

The first large-scale multidisciplinary oceanographic study of the Malin shelf/slope area, the Shelf Edge Study (SES), was conducted between March 1995 and September 1996 (Souza et al., 2001). The observational area covered a rectangle with meridional range from 55°N to 58°N, and zonal range from 8°W to 10°W. The intensity, spatial structure, and temporal variability of the slope current were recorded at a number of moorings using Acoustic Doppler Current Profilers (ADCP). It was found that the slope current in the area was predominately barotropic with velocity in the core around $0.2\,\mathrm{m\,s^{-1}}$. The flow was stronger in winter than in other seasons. The cross-slope velocity was typically at the level of $0.02\,\mathrm{m\,s^{-1}}$ in summer and $0.04\,\mathrm{m\,s^{-1}}$ in winter.

Quite useful information on the spatial characteristics of the slope current around the Hebrides was obtained during the ARGOS tracked drifter experiment (Burrows and Thorpe, 2002). A number of drifters with drogues at 50 m depth were released over the slope at $56°15'$N on a line between the 200 m and 1000 m isobaths. Based on the drifters' trajectories, the slope current was initially directed poleward along the continental slope in a laterally constrained jet-like flow. Depending on the position with respect to bathymetry, the recorded slope current velocity ranged from 0.05 to $0.7\,\mathrm{m\,s^{-1}}$.

The most recent measurements of the slope current were obtained in July 2013 during the JC88 cruise aboard the RRS "James Cook" as part of the NERC-funded project, Fluxes Across Sloping Topography in the North-east Atlantic (FASTNEt). A number of moorings equipped with ADCPs were deployed along the slope as shown in Figure 1 with the aim of resolving the coherence of the slope current as it encountered a canyon orientated perpendicular to the slope. Vertically averaged ADCP time series recorded at Lb, Sb, and Sd moorings are presented in Figure 2. They reveal a dominant tidal periodicity in all recorded time series with a superposition of semi-diurnal and diurnal tidal harmonics (panel SD in Figure 2, for instance) which we refer to as diurnal intermittency. The TPXO8.1 model output calculated for the positions of mooring deployment and presented to the right in Figure 2 shows quite consistent intensity of the observational and model predicted tidal signals with obvious diurnal intermittency. The only significant difference between observational and predicted time series is the presence of quasi-stationary currents recorded at the moorings. Low pass 25 h running average filtering of the depth-averaged time series revealed a residual current with a velocity of between 0.05 and $0.2\,\mathrm{m\,s^{-1}}$ (the red lines in Figure 2).

In addition to moorings, a number of drifters were released in the area during the JC88 experiment. Analysis of the drifters' tracks has also confirmed the presence of the along-slope current with maximum velocities up to $0.2\,\mathrm{m\,s^{-1}}$ (find drifter tracks shown in Figure 1 by red, green, and blue lines).

During a dye release experiment that sought to identify the circulation associated with the slope current, a cross-slope transect was completed whilst tow-yoing a microstructure profiler behind the ship at approximately 1 knot. The position of the transect is indicated by the red straight line in Figure 1. The vessel-mounted RDI 75 kHz Ocean Surveyor broadband acoustic Doppler current profiler (VMADCP) data collected during this transect provides information on the cross-slope structure of the depth-dependent currents. Horizontal currents were measured with a 5 second ping interval in 16 m bins. We present here the 2 minute short-term averaged data which have subsequently been cleaned with a 7 point median filter and smoothed with a 5 point running average over both time and depth (Figure 3 b). **Shallow-water conditions at the transect (400-700 metre depth) allowed bottom-tracking of the ship's position. This fact was used for cal-**

culations of an absolute velocity relative to the Earth using the method described in Joyce (1989) in which the raw data were corrected by misalignment angle (0.1874°) and amplitude scaling factor (1.000816).

The vessel completed the transect downstream of the wall of the canyon during 7.43 hours on 13th July 2013. The dye release targeted the slope current core that was found in a water depth of 600 m. The dye moved into water of 800 m depth such that the transect extended from the upper slope ($\leq$200 m depth) to depths $\geq$1000 m after crossing the canyon.

Within the transect, the poleward current is intensified near the bed in the slope region. A core of the slope current is located above the bed in the area of 400 m isobath, Figure 3 b. The figure represents both spatial and temporal variability of the velocity field and is thus difficult to interpret when the tidal signal and slope currents are comparable. Note, however, the time series of tidal currents predicted by the TPXO8.1 tidal model (Egbert and Erofeeva, 2002) for the time span 15:00-22:00 on 13 July 2013 at the similar positions of the vessel across the slope, Figure 3 a, clearly shows barotropic tidal velocity below 0.05 ms^{-1}, which implies that Figure 3 b can be treated as observational evidence of slope current. Thus, no filtering of the tidal signal is required in order to identify the slope current with velocity 0.2 $\mathrm{m\,s}^{-1}$ which is clearly seen in Figure 3 b.

Note that the velocity field obtained using the VMADCP data, Figure 3 b, can be aliased by tidally generated internal waves. This effect is a matter of great concern in areas of strong bottom currents, specifically, at positions of tidal beam generation. The model

predicted amplitude of horizontal velocity of the along-slope current presented in Figure 3 c shows that the area with strong tidal activity does not coincide with the position of intensification of the bottom current found from the VMADCP data.

3. Numerical solution for the Malin Sea slope current

The MITgcm was applied to investigate the Malin Sea slope current. The model domain is shown in Figure 1. The grid resolution was 150 m in the horizontal and 10 m in the vertical directions. Eight principal tidal harmonics were activated in the model in the right hand side of the momentum balance equations. The parameters of tidal forcing were taken from the TPXO8.1 inverse tidal model (Egbert and Erofeeva, 2002) and using the ADCP time series recorded during the JC88 experiment, Figure 2. The parameters of the tidal current discharge and tidal phases of each harmonic are presented in the Table.

The vertical turbulent closure for the coefficients of vertical viscosity ν and diffusivity κ was provided by the Richardson number dependent parametrisation, PP81, (Pacanowski and Philander, 1981):

$$\begin{aligned} \nu &= \frac{\nu_0}{(1+\alpha\mathrm{Ri})^n} + \nu_b, \\ \kappa &= \frac{\nu}{(1+\alpha\mathrm{Ri})} + \kappa_b. \end{aligned} \tag{1}$$

Here Ri is the Richardson number, $\mathrm{Ri} = N^2(z)/(u_z^2 + v_z^2)$, and $N^2(z) = -g/\rho(\partial\rho/\partial z)$ is the buoyancy frequency (g is the acceleration due to gravity, and ρ is the density), u and v are the components of horizontal velocity; ν_b=10^{-5} m^2 s^{-1} and κ_b=10^{-5} m^2 s^{-1} are the background parameters,

ν_0=1.5·10^{-2} m^2 s^{-1}, α=5 and n=1 are the adjustable parameters. Such a parametrisation increases coefficients ν and κ in the areas where the Richardson number is small which should take into account the mixing processes induced by the shear instabilities and breaking internal waves. We set no-slip boundary condition for the velocities at the bottom without activation of any bottom drag parametrisation.

The model was run for five days in order to spin-up all tidally induced processes. Barotropic and baroclinic responses were investigated separately. The fluid stratification for the baroclinic mode was taken from CTD profiles acquired during the JC88 observations. The buoyancy frequency profile for these experiments was averaged over all CTD stations conducted in the area. It is shown in the inset in Figure 1.

The primary target of these numerical experiments was the identification of the residual currents generated by tides. The residual currents were calculated by averaging the model output over four days; for transects 1-3 depicted in Figure 1 the residual currents are shown in Figure 4. The baroclinic response is shown in the left column, and the barotropic response to the right.

Both barotropic and baroclinic outputs demonstrate evidence of a poleward water flux with maximum velocity of 0.2 ms^{-1} in the area of the shelf break. A comparison of the barotropic and baroclinic cases reveals the predominance of the barotropic component, as was also found by Souza et al. (2001). An intermediate conclusion from these experiments is that setting the tidal potential as the only forcing in the numerical model leads to the formation of a northward directed residual current in the Malin Sea slope/shelf area. In order to make our analysis more general in terms of hydrodynamic conditions, we aim to find an analytical solution for a tidally induced slope current that can be applicable for a wide range of input parameters.

4. Analytical solution for a tidally generated slope current

Consider a two-dimensional slope-shelf bottom topography $H(x)$ with isobaths parallel to the $y-$axis directed to the north and eastward $x-$axis directed across the isobaths. The upward looking vertical $z-$axis starts at the free surface. With such an arrangement the depth-averaged momentum balance equations in hydrostatic approximation with linear dissipation read:

$$\begin{aligned}\frac{\partial u}{\partial t} + u\frac{\partial u}{\partial x} - fv &= -g\frac{\partial \zeta}{\partial x} - \frac{ku}{H}, \\ \frac{\partial v}{\partial t} + u\frac{\partial v}{\partial x} + fu &= -\frac{kv}{H},\end{aligned} \tag{2}$$

It is assumed here that there is no pressure gradient applied along the slope, and that all variables are a function of the cross-slope coordinate x and time t only. In these equations $u(x,t)$ and $v(x,t)$ are depth-averaged horizontal velocities, $\zeta(x,t)$ is the surface elevation, $H(x)$ is the water depth, f is the Coriolis parameter, g is the acceleration due to gravity, and $k(x)$ is a friction coefficient.

We assume that developing dynamical processes are a superposition of tidal motions (superscript t) and a stationary slope current (superscript c):

$$\begin{aligned}u &= u^t + u^c, \\ v &= v^t + v^c, \\ \zeta &= \zeta^t + \zeta^c.\end{aligned} \tag{3}$$

Tidal currents u^t and v^t are periodic functions

$$\begin{aligned} u^t &= a\cos(\omega t - \phi_a), \\ v^t &= b\cos(\omega t - \phi_b), \end{aligned} \tag{4}$$

where a, ϕ_a and b, ϕ_b are amplitudes and phases of u^t and v^t velocities, respectively, and ω is the tidal frequency.

After substitution of (3) into (2) and averaging over one tidal cycle the governing system is reduced to the following:

$$\begin{aligned} \langle u^t \frac{\partial u^t}{\partial x}\rangle - f\langle v^c\rangle + g\langle \frac{\partial \zeta^c}{\partial x}\rangle &= 0, \\ \langle u^t \frac{\partial v^t}{\partial x}\rangle &= -\frac{\langle k v^c\rangle}{H} \end{aligned} \tag{5}$$

Here $\langle\rangle$ means temporal averaging. In the derivation of (5) it was assumed that the cross topography water transport is negligibly small, i.e. $\langle u^c\rangle \approx 0$.

The velocity of the along-slope rectified flow $\langle v^c\rangle$ can be found from the second equation of system (5). After the definition of $\langle v^c\rangle$ the free surface elevation $\langle \zeta^c\rangle$ can be derived from the first equation. Taking into account that the amplitudes a and b of tidal velocities (3) are depth dependent, it is sensible in further analysis to operate with the tidal discharges $U^t = u^t H$, $V^t = v^t H$ instead of velocities u^t and v^t:

$$\begin{aligned} U^t &= aH\cos(\omega t - \phi_a) &= A\cos(\omega t - \phi_a), \\ V^t &= bH\cos(\omega t - \phi_b) &= B\cos(\omega t - \phi_b). \end{aligned} \tag{6}$$

Note also that in long tidal waves the amplitudes of water discharge A and B are less sensitive to the water depth, so one can assume here their invariance for the whole slope-shelf area (non-divergent tidal wave, $\nabla\cdot(H\vec{u^t}) = 0$, where $\vec{u^t} = (u^t, v^t)$).

After averaging the left hand side of the second equation, (5) reads

$$\langle u^t \frac{\partial v^t}{\partial x} \rangle = -\frac{AB\cos(\phi_a - \phi_b)}{2} \frac{1}{H^3} \frac{\partial H}{\partial x}.$$

According to Loder (1980), the linear friction coefficient k does not depend on time but it is spatially variable, i.e. $k(x) = C_D\sqrt{A^2 + B^2}/H(x)$, where C_d is a drag coefficient. With this assumption the second equation of system (5) is reduced to

$$\langle v^c \rangle = \frac{AB\cos(\phi)}{2C_D\sqrt{A^2 + B^2}} \frac{1}{H} \frac{\partial H}{\partial x}. \tag{7}$$

Here $\phi = \phi_a - \phi_b$ is the phase lag between u^t and v^t tidal velocities.

5. Numerical investigation of tidally induced slope currents

In this section we check the applicability of the analytical solution (7) to real oceanographic conditions. As a test bed for the analysis we took a topography profile averaged over the whole model domain shown in Figure 1 and approximated it by a sine function as follows

$$H(x) = 1500 - 1300 \cdot \sin^2(\pi(x - L)/2L). \tag{8}$$

Here $0 \leq x \leq L$, L is the measure of the topography width. The obtained two-dimensional bottom profile was extended in the $y-$direction for 75 km, so the new model domain covered the area $75{\times}75\,\mathrm{km}^2$.

A series of numerical experiments was conducted for a wide range of input parameters of tidal discharge, topography scale, tidal ellipses orientation, stratification, and tidal frequency. At the first stage we compared the analytically predicted slope current with the model output for L =24 km (the basic case run, hereafter BCR). The tidal forcing was limited to only the

M_2 tidal harmonic. The amplitudes of tidal discharge were A=100 m^2 s^{-1} and B=40 m^2 s^{-1}, the phase lag ϕ =114° that corresponds to cos(ϕ) =-0.41 (stronger and weaker tidal forcing as well as different phase lags are discussed in sensitivity runs). The water stratification was taken as that shown in the inset to Figure 1. The model was run for ten tidal periods, and the residual currents were found from the last four tidal periods by time averaging.

5.1. Basic Case Run (BCR)

The results of the BCR are presented in Figure 6. Panel a) shows the 3D structure of the residual current flowing northward. The track of an ad hoc model drifter drogued at 70 m depth (shown in blue) depicts the trajectory of water particles. The tidal current that generates the residual flow is shown in Figure 6 b as a tidal ellipse at the 485 m isobath. Velocity amplitudes for this ellipse were recalculated using the discharge values.

Figures 6 c and 6 d show the cross-slope time averaged distributions of vertical viscosity and diffusivity coefficients predicted by the PP81 parametrisation (1). It was found that numerical coefficients ν and κ are consistent with that measured over the Malin shelf break area by Inall et al. (2000). They found that the largest tidally averaged values of vertical eddy diffusivity were at the level of 12 $\times 10^{-4}$ m^2 s^{-1} in a vertically integrated 100 m thick bottom boundary layer (BBL). A similar value calculated by averaging the MITgcm output is shown in Figures 6 c and 6 d and is equal to $\bar{\nu}$=10 $\times 10^{-4}$ m^2 s^{-1}. This consistency suggests that the set of adjustable parameters taken in (1) is good enough to reproduce the background mixing correctly.

Having the BC run as a reference point for further calculations, we can now investigate the slope current generated for a wide range of input parameters in order to compare the model predicted velocities with the analytical solution (7).

5.2. *Effect of topography*

We start the comparative analysis by considering the sensitivity of the generated slope current to the width of the topography. The velocity fields calculated for L=24, 42, and 60 km of profile (8) are presented in Figure 7. Comparing panels a-c it is clear that the slope current weakens with an increase of the topography width L. This result is in agreement with formula (7) which predicts the slope current dependence on the bottom topography as $\frac{1}{H(x)}\frac{\partial H(x)}{\partial x}$.

Another conclusion from Figure 7 a-c is that the model predicted slope current is a superposition of barotropic and baroclinic modes. It resembles a barotropic flow being mostly located over the shelf break, however, vertical variability of the current is also apparent.

It is worth mentioning here that analytical solution (7) was developed using vertically averaged equations (2), but the MITgcm numerical solution is based on the full set of primitive equations. To make the comparative analysis more accurate, it is sensible to compare the depth integrated numerical velocities as well, i.e.

$$\bar{v}(x) = \frac{1}{H(x)}\int_{-H(x)}^{0} v dx. \tag{9}$$

The blue lines in Figures 7 d-f show normalised profiles of the bottom term $\frac{1}{H(x)}\frac{\partial H(x)}{\partial x}$ that appears in (7), and the vertically averaged, model predicted, normalised velocity $\bar{v}(x)$ is shown in red. It is seen that three pairs of curves coincide nearly perfectly on the shelf including the positions of their maxima.

In the deep part of the basin the discrepancy between two solutions is obvious, and this difference increases with the increase of L.

In the theory presented in Section 4 there is an uncertainty in setting the value of the drag coefficient C_d. In different hydrodynamical applications it varies over quite a wide range. The bottom friction for a propagating sinusoidal wave was first investigated by Putnam and Johnson (1949) who found an equation that defines the change of the wave energy depending on the parameters of wave and topography. Bretschneider and Reid (1954) applied this equation to the Gulf of Mexico and found C_d=0.01. Hasselmann and Collins (1968) calculated C_d=0.015 for the area offshore Florida assuming a Gaussian type of surface wave spectrum. In the most recent study Warner et al. (2013) used pressure sensors for measuring currents over rough topography at the Puget Sound, Washington. They found that the drag coefficient should be at the level of 9×10^{-2}.

In fact, one should distinguish the drag coefficient calculated based on the observational data discussed above from that used in modelling. In numerical circulation models, the drag coefficient C_d is normally taken in the range C_d=0.0025-0.005. According to Blumberg and Mellor (1987) its value depends on the grid size, von Karman constant and local bottom roughness. The usage of the bottom friction parameterization in circulation models with coarse vertical resolution is necessary to introduce a sink of energy in the BBL which is not reproduced in the models directly. However, in cases with fine resolution vertical grid (Δz = 5-10 m) the BBL and its damping effect can be resolved.

Note, that the purpose of the present study is to investigate the slope currents and to validate formula (7). In doing so, it is suggested here to calibrate the analytical solution by finding the drag coefficient C_d that reveals the best fit between formula (7) and the model output. If the values of the drag coefficient C_d are consistent over a wide range of input parameters (which is the case, see below), one can then recommend the use of this C_d value for all further oceanographic applications on the investigation of tidally induced slope currents.

The procedure of defining the C_d coefficient can be as follows. The MITgcm predicted vertically averaged velocity is substituted into the left hand side of formula (7). The numerical velocity is taken at the point where $\mid \frac{1}{H(x)} \frac{\partial H(x)}{\partial x} \mid$ has its maximum. As it was shown above, the positions of the maximums of the model velocity and the bottom term $\frac{1}{H(x)} \frac{\partial H(x)}{\partial x}$ coincide, Figure 7 d-f. After that C_d is calculated using formula (7).

As it is seen from the bottom panels of Figure 7, the suggested method works reasonably well in the considered case. Specifically, the values of the drag coefficient in all three cases are quite consistent, i.e. C_d =0.014 for the BCR, and C_d =0.012 for two other considered cases.

5.3. Influence of stratification and tidal frequency

There are a few more points we have to pay attention to in our analysis. First of all, formula (7) was developed for a homogeneous fluid, but slope currents can be sensitive to fluid stratification. Another point is that the tidal frequency ω is not included in the analytical solution (7), which confirms the independence of the slope current to this parameter. The aim of the next series of experiments was to clarify the role of stratification and tidal frequency in setting the tidally driven slope currents. The bottom topography in these experiments was the same as in the BCR.

Figure 8 shows cross-slope transects of residual currents for the M_2 tide (a,b) and K_1 tide (c, d) in stratified (a, c) and homogeneous (b, d) fluids. It is seen that the core of the slope current in homogeneous fluid is mostly uniform in the vertical direction for both tidal frequencies. However, the K_1 current occupies a slightly larger area than M_2 current and its maximum velocity $\bar{v}_{\max}$=0.1 m s^{-1} slightly exceeds the similar velocity of $\bar{v}_{\max}$=0.085 m s^{-1} generated by the semi-diurnal tide.

The comparison of stratified and homogeneous fluid cases shows that the slope currents are mostly barotropic (Figure 8), although fluid stratification introduces some distortions into the residual flows; the core of of the stratified slope currents are not vertical but slightly tilted. The direction of inclination depends on tidal frequency: in the case of the M_2 tide it is inclined towards the shelf, but for the K_1 tide it is inclined towards deep water. It is interesting that for the M_2 tide the maximum of the current velocity $\bar{v}_{\max}$ in stratified fluid is smaller than in homogeneous fluid, but this is quite opposite for the K_1 tide. Note, however, that all these variations do not exceed 20%. The value of the drag coefficient C_d in this series of experiments was found to be from 0.01 to 0.014.

5.4. Sensitivity to the tidal discharge

We continue the validation of formula (7) with the analysis of the sensitivity of the analytical and numerical solutions to the tidal discharge. In formula (7) the latter appears as a nonlinear term $AB/\sqrt{A^2+B^2}$. If solution (7) is correct, then the increase or decrease of both amplitudes, A and B, in the forcing term for the numerical model should lead to a similar tendency in intensity of the rectified flows.

This statement was tested in a series of numerical experiments with different values of discharge A and B. The cross-slope transects of the residual along-topography current calculated for three different values of the discharge A and B are shown in Figure 9. It is seen that the spatial structure of the slope current in all cases is nearly identical. However, in terms of intensity, a twofold increase or decrease of A and B values compared with the BCR results in a nearly similar response of the slope current maximum. The values $\bar{v}_{\max}$ for the three panels shown in Figure 9 (from left to right) are $0.2\,\mathrm{m\,s^{-1}}$, $0.079\,\mathrm{m\,s^{-1}}$ (BC run), and $0.036\,\mathrm{m\,s^{-1}}$. In other words, a twofold increase or decrease of the tidal forcing leads to an increase of 2.5 times ,or a decrease of 2.2 times, the values of the maximum velocity, respectively.

Finally, we found that the best fit between analytical and numerical solutions takes place when C_d is equal to 0.011, 0.014, and 0.016 in three considered cases, which is consistent with the values obtained in previous experiments, see Figures 7 and 8.

5.5. Sensitivity to the phase lag and direction of the velocity vector rotation

Another parameter that should be investigated in the validation of formula (7) is the phase lag $\phi = \phi_a - \phi_b$ between the tidal velocities u^t and v^t, see (4). In the BCR the function $\cos(\phi)$ returns the value -0.41. In conjunction with the negative term of the bottom function $\frac{1}{H(x)}\frac{\partial H(x)}{\partial x}$ the analytical solution (7) predicts a positive slope current directed northward, which is confirmed by the MITgcm control runs.

It is worth mentioning here that two principal parameters of the tidal stream (4), i.e. the tidal phases ϕ_a and ϕ_b, do not show explicitly the inclination of the tidal ellipse γ, see Figure 10. It thus appears sensible for further analysis to find an explicit relationship between the phase lag and tidal ellipse inclinations.

To present the tidal stream in terms of tidal ellipses let us operate with the tidal current as a complex function:

$$w = u^t + iv^t, \tag{10}$$

where $i = \sqrt{-1}$. After substitution of (4) into (10) and conducting a series of routine mathematical procedures one can present w as a sum of two vectors rotating in opposite directions, see Figure 10:

$$w = \frac{W_a}{2}\exp[i(\omega t + \theta_a)] + \frac{W_b}{2}\exp[-i(\omega t - \theta_b)]. \tag{11}$$

Here

$$\begin{aligned}
W_a &= \sqrt{a^2 + b^2 + 2ab\sin(\phi_b - \phi_a)}, \\
W_b &= \sqrt{a^2 + b^2 - 2ab\sin(\phi_b - \phi_a)}, \\
\theta_a &= \arctan\left[\frac{-a\sin(\phi_a) + b\cos(\phi_b)}{a\cos(\phi_a) + b\sin(\phi_b)}\right], \\
\theta_b &= \arctan\left[\frac{a\sin(\phi_a) + b\cos(\phi_b)}{a\cos(\phi_a) - b\sin(\phi_b)}\right].
\end{aligned} \tag{12}$$

When two circular radial vectors are aligned in the same direction, the tidal current reaches its maximum. It is clear from (11) that this situation happens when $\omega t + \theta_a = -\omega t + \theta_b + 2k\pi$, where $k = 0, \pm 1, \pm 2, \ldots$. This relation gives the moment of time when the maximum is achieved:

$$t_{\mathrm{max}} = \frac{\theta_a - \theta_b}{2\omega} + \frac{k\pi}{\omega}. \tag{13}$$

The velocity vector (11) at this moment of time is expressed as follows

$$w_{\max} = \frac{W_a + W_b}{2} \exp\left(i\frac{\theta_a + \theta_b}{2} + k\pi\right), \tag{14}$$

The vector length $|w_{\max}|$ in terms of the tidal stream parameters a, b, and ϕ reads

$$|w_{\max}| = \frac{1}{2}\left(\sqrt{a^2 + b^2 + 2ab\sin\phi} + \sqrt{a^2 + b^2 - 2ab\sin\phi}\right). \tag{15}$$

Finally, the angle γ with respect to $0x$ axis (see Figure 5) is:

$$\begin{aligned}
&a > b \\
&\gamma = \frac{1}{2}\arctan\left[\frac{2ab\cos\phi}{a^2 - b^2}\right] + n\pi, \quad \begin{cases} n = 0 & \text{if} \quad \cos\phi > 0 \\ n = 1 & \text{if} \quad \cos\phi < 0 \end{cases} \\
&a < b \\
&\gamma = \frac{1}{2}\arctan\left[\frac{2ab\cos\phi}{a^2 - b^2}\right] + \frac{\pi}{2}.
\end{aligned} \tag{16}$$

Here the phase lag $\phi = \phi_a - \phi_b$.

Formula (16) presents the relationship between the phase lag ϕ and the tidal ellipse inclination γ. An obvious conclusion from this analysis is that if the phase lag ϕ exceeds $\pi/2$, i.e. $\cos\phi$ is negative, then the inclination angle γ exceeds $\pi/2$. In this case formula (7) predicts the slope current as being directed northward. Alternatively, the slope current should flow southward when $\gamma < \pi/2$ (when $\cos\phi > 0$).

The principal outcome from this analysis is the relationship (16) between the phase lag ϕ and the ellipse inclination γ. If the value of $\cos\phi$ does control the direction of the slope current as the analytical solution predicts, a similar tendency should also be found in the numerical model output.

A series of numerical experiments was conducted to study the sensitivity of the slope current to the phase lag ϕ (or tidal ellipse inclination γ) and the direction of the tidal current vector rotation. A comparison of Figures 11 a, 11 a_1 calculated for $\cos\phi$=-0.41 ($\phi = -114°$, the BCR), with Figures 11 b, 11) b_1, for $\cos\phi = 0.41$ ($\phi = -63°$) confirms the hypothesis that the model is sensitive to the parameter $\cos\phi$. In case $\cos\phi = -0.41$ and $\cos\phi$=0.41 it reproduces nearly the same residual current but flowing in the opposite directions.

Note, however, that two compared vertical cross-sections are not fully asymmetric. The core in the BCR current is inclined on-shelf, whereas the south directed current is inclined off-shore. In addition, its maximal velocity $\bar{v}_{\max}$ =0.087 m s^{-1} slightly exceeds $\bar{v}_{\max}$ =0.079 m s^{-1} found for the BCR, although the calculated drag coefficient C_d values are nearly the same.

Input parameters in the two considered cases were the same except for the phase lag ϕ. The latter, in fact, controls the inclination of the tidal ellipse (see, for instance, Figures 11 a, and 11 b). It also sets the direction of the velocity vector rotation. Negative values in the range $-\pi < \phi < 0$ result in clockwise rotation, but a positive phase lag $0 < \phi < \pi$ produces counter-clockwise rotation. Taking into account that the cosine is a symmetric function, i.e. $\cos(\alpha) = \cos(-\alpha)$ for any angle α, formula (7) predicts that the residual current should be independent of the velocity vector rotation.

The confirmation of this conclusion is shown in Figure 11 c which represents the model predicted slope current calculated for $\phi = 114°$. As the analytical formulae (7) predicts, the MITgcm produces nearly identical results to the BCR for both clockwise and counter-clockwise rotated velocity vectors (compare Figure 11 a and 11 c). The direction of the two currents and their spatial structure are similar although the maximum velocities are slightly different, i.e. $\bar{v}_{\max}$ =0.074 m s^{-1} for the last case, and 0.079 m s^{-1} for the BCR. The drag coefficients in both cases are nearly the same.

The next test of the analytical solution also concerns the analysis of its sensitivity to the combination of the tidal discharges A and B in Ox and Oy directions, respectively. Formula (7) predicts that the slope current should be identical in cases when the term, $AB/\sqrt{A^2+B^2}$, has the same value, regardless $A > B$ or vice versa. The next numerical experiment was conducted with A =40 m^2 s^{-1}, B =100 m^2 s^{-1}, Figure 11 d, (instead of A =100 m^2 s^{-1}, B =40 m^2 s^{-1}, as in the BCR) and $\cos\phi$=-0.41. Figure 11 d$_1$ shows the northward generated slope current with maximum velocity $\bar{v}_{\max}$ =0.1 m s^{-1}, which slightly exceeds $\bar{v}_{\max}$=0.079 m s^{-1} calculated for the BCR, and returns the drag coefficient C$_d$=0.011. Note that the orientation of tidal ellipses with respect to the bottom in two considered cases is completely different (compare Figures 11 a and 11 d).

All numerical experiments discussed so far were conducted with $\cos\phi = \pm 0.41$. Formula (7) predicts strong sensitivity of the slope current characteristics to the phase lag ϕ. Two extra runs were performed with $\cos\phi$=-0.866 and $\cos\phi$=0. They are presented in Figures 11 e, e$_1$ and 11 f, f$_1$, respectively. All other input parameters were kept the same as in the BCR. It is seen that when the cosine of the phase lag changes from -0.412 to -0.866, the mean velocity $\bar{v}_{\max}$ is nearly doubled from 0.079 m s^{-1}, as in the BCR (see Figure 11 a$_1$), to 0.157 m s^{-1}. However, the drag coefficient C$_d$ remains nearly the same in the whole range coinciding with the BCR value.

The numerical experiment conducted with $\cos\phi$=0 (inclination γ=0) also confirms formula (7): no slope current is generated by the MITgcm when $\cos\phi$=0, see Figure 11 f, f_1.

5.6. Coordinate transformation

Formula (7) was derived for the bottom topography oriented in the meridional direction with u-velocity directed across and v-velocity along the isobaths. However, in reality the continental slope can be oriented randomly. To generalise the analytical solution for an arbitrarily oriented bottom consider a simple topography scheme as that shown in Figure 12. To make analytical solution (7) applicable to this situation, the coordinate system should be rotated clockwise by the angle β, Figure 12. The analysis below shows the relationship between the tidal ellipse parameters in the new and old coordinate systems.

The task is to transform the topography to a new coordinate system (O, x_r, y_r, z_r) by a simple rotation of the coordinate system (O, x, y, z) by an angle β. The relationship between two coordinate systems reads:

$$\begin{bmatrix} x_r \\ y_r \end{bmatrix} = \begin{bmatrix} \cos\beta & \sin\beta \\ -\sin\beta & \cos\beta \end{bmatrix} \begin{bmatrix} x \\ y \end{bmatrix}. \tag{17}$$

Applying (17) to vector (4), the components u_r^t and v_r^t of the tidal flow in the new co-ordinate system are:

$$\begin{aligned} u_r^t &= a_r \cos(\omega t - \phi_{ar}), \\ v_r^t &= b_r \cos(\omega t - \phi_{br}), \end{aligned} \tag{18}$$

where

$$
\begin{aligned}
a_r &= \sqrt{a^2\cos^2\beta + b^2\sin^2\beta + 2ab\sin(2\beta)\sin(\phi_b - \phi_a)}, \\
b_r &= \sqrt{a^2\sin^2\beta + b^2\cos^2\beta - 2ab\sin(2\beta)\sin(\phi_b - \phi_a)}, \\
\phi_{ar} &= \arctan\left[\frac{a\cos\beta\sin(\phi_a) + b\sin\beta\sin(\phi_b)}{a\cos\beta\cos(\phi_a) + b\sin\beta\cos(\phi_b)}\right], \\
\phi_{br} &= \arctan\left[\frac{-a\sin\beta\sin(\phi_a) + b\cos\beta\sin(\phi_b)}{-a\sin\beta\cos(\phi_a) + b\cos\beta\cos(\phi_b)}\right].
\end{aligned}
\tag{19}
$$

Using (15) and (19) one can find for the major X and minor Y axis of the tidal ellipse, as well as for the ellipse inclination angle γ (see Figure 10) the following

$$
\begin{aligned}
X_r &= X, \\
Y_r &= Y, \\
\gamma_r &= \gamma - \beta.
\end{aligned}
\tag{20}
$$

Thus, the major and minor axis of the tidal ellipses in the new and old coordinate system coincide, although the new inclination angle should be corrected by the additional angle β. The angle of rotation β can be positive or negative depending on the direction of rotation: β is positive in the case when the coordinate system is rotated counter-clockwise and negative when it rotates clockwise.

6. Analysis of the Malin Shelf slope current

The upgraded formula (7) that takes into account the coordinate transformation was applied to the Malin shelf/slope area presented in Figure 1.

As it was shown above, the position of the core of the slope current in formula (7) is controlled by the term $\frac{1}{H}\frac{\partial H}{\partial x}$. The spatial distribution of the bottom term value shown in Figure 13 a, points out that its largest absolute value is located in the area above the 400 m isobath. The white line in Figure 13 a shows a smoothed isobath profile that was used to calculate the angle of rotation β at every single point.

Substituting the discharge values for the M_2 tide from the Table and after the coordinate transformation, formula (7) predicts the residual tidal velocity shown in Figure 13 b. The slope current is located in quite a narrow band; it is stronger in the northern part of the model domain. Similar results but for the depth integrated values of the along-slope current predicted by the MITgcm are shown in Figure 13 c. The comparison of both figures shows their consistency, both for the current position, and for its strength, although the model predicted residual flow occupies a slightly larger area.

The stability of barotropic slope currents $\bar{v}$ similar to that presented in Figure 13 was discussed by Li and McClimans (2000). They found that stability of $\bar{v}$ is controlled by the following cross-slope function:

$$\chi = \frac{1}{H}\frac{\partial H}{\partial x}\left(f + \frac{\partial \bar{v}}{\partial x}\right) - \frac{\partial^2 \bar{v}}{\partial x^2}.$$

The current is stable when χ is positive or negative, but it loses its stability when χ changes sign across the jet. In our case χ is negative everywhere in the Malin Sea slope area and thus the current $\bar{v}$ is proven to be stable.

7. Discussion and conclusions

The theoretical analysis of tidally rectified slope currents (Section 4) presented here is a part of the theory developed by Huthnance (1973), Loder

(1980), and Zimmerman (1980). In particular, Huthnance (1973) considered tidally rectified flows as a result of a balance between drag terms and the net momentum transport into a region. To find a solution, a perturbation theory that included multiple tidal harmonics was applied to vertically averaged shallow water equations. It was found that the speed of the residual current is proportional to the slope of the bottom. Unfortunately, the final formula of Huthnance (1973) solution did not include the tidal ellipse parameters explicitly, which is why its practical application is not straightforward. In addition, the solution contains a term with the ratio of frictional to inertial forces, whose estimation is not always obvious.

Loder (1980) modified the theory by including a feedback of the generated residual currents to the tidal velocity fields. He obtained an analytical solution for the stepwise bottom profile that was by Huthnance (1973). The complete version of the solution included not only the principal tidal constituent with frequency ω, but also took into account its nonlinear interaction with multiple 2ω and 3ω tidal harmonics. Zimmerman (1980) generalised the theory to the case of an arbitrary bottom profile. His solution is based on a number of special mathematical functions which makes its practical application a little cumbersome with not always transparent final results.

Surprisingly, the simplified theory presented in Section 4 captures very well all of the main features of the tidally rectified flows over the slope though it does not account for higher harmonics. Formula (7) is relatively simple; however, as it was shown above, it predicts properties and quantitative characteristics of the MITgcm replicated slope currents quite accurately. Its most striking feature is that the direction and strength of the rectified flow is mostly controlled by the phase shift ϕ between the u^t and v^t tidal components, which along with the amplitudes of the velocity components a and b, formula (4), set the tidal ellipse inclination γ (see formulae (16)).

A convincing example of the fundamental sensitivity of the rectified flows to the phase shift ϕ is shown in Figures 11 a and 11 b. An absolute value of $\cos(\phi)$ in both cases is the same, but signs are opposite. In such a situation, formula (7) predicts that the residual current in both cases must have the same in structure but should flow in opposite directions. Importantly, the same behaviour is also demonstrated by the MITgcm which produces slope currents flowing in opposite directions when $\cos(\phi)$ changes sign. Note, that the MITgcm is a fully nonlinear nonhydrostatic model which is free from most assumptions used in modelling. In light of the results found above, the consistency between the model output and the analytical solution looks promising.

A reasonable explanation of the sensitivity of the slope current direction to the sign of $\cos(\phi)$ can be found in terms of equations (5). With the assumptions of stationarity of the residual flow and zero meridional pressure gradient, the only term remaining in the left-hand-side of the second equation (5) is the residual advection of the v-momentum in x-direction, $\langle u^t \frac{\partial v^t}{\partial x} \rangle$. Given that u^t and v^t are defined by formula (6) we have

$$u^t \frac{\partial v^t}{\partial x} \sim \cos(\phi_a - \phi_b) + \cos(2\omega t - \phi_a - \phi_b)$$

In this equation the time averaging of the second term gives a zero result, which means that the residual momentum advection depends on the phase shift $\phi = \phi_a - \phi_b$ (on $\cos\phi$ to be more specific) that controls the ellipse inclination γ, equation (16). In the time-averaged equation (6), it can be compensated by the dissipative term $-\dfrac{\langle kv^c\rangle}{H}$ in which the slope current v^c is included linearly.

For negative values of the bottom derivative $\partial H/\partial x$, v^c is positive when $\frac{1}{2}\cos\phi$ is negative and the ellipse inclination γ exceeds 90°, which is also clearly demonstrated in the MITgcm output (Figures 11 a and 11 b). It is important that no restrictions, except of a two dimensionality of the bottom topography, were introduced into the numerical model, but consistency between theoretical and numerical results is obvious.

The theory presented in Section 4 is formally valid for a standard tidal (west-north) co-ordinate system with meridionally oriented topography and tidal amplitudes a, b and tidal phases ϕ_a and ϕ_b taken from any prediction tidal model, TPXO8.1, for instance. That makes such applications quite straightforward. Note, however, that in reality isobaths are oriented randomly. In such situations, the orientation of isobaths with respect to tidal ellipses would be a more representative parameter for making an operational oceanographic prognosis. Subsection 5.6 provides all necessary details for the co-ordinate transformation that allows application of formula (7) (with obvious corrections related to tidal ellipse-topography orientation) to all possible oceanographic situations.

One of the principal outcomes from this analysis is the high level of consistency of the drag coefficient C_d found in a wide range of input parameters. In all experiments considered above the drag coefficient C_d varied in the range between 0.01 and 0.016. Thus, with a 95% confidential interval one can recommend the usage of C_d=0.0128±0.0012. Applied to the Malin shelf/slope area, formula (7) predicted a slope current with maximum velocity up to

$0.08\,\mathrm{ms}^{-1}$. The MITgcm generated a similar rectified flow, which justifies application of formula (7) to many other regions worldwide.

Acknowledgements

This work was supported by the Natural Environment Research Council grants FASTNEt (award NE/I030259/1) and Deep Links (award NE/K011855/1). We thank two reviewers, especially Dr. Andrew Dale, for their attention to this paper and a number of valuable comments.

References

Blumberg, A. F., and G.L. Mellor (1987) A description of a three-dimensional coastal ocean circulation model. Three dimensional ocean models (N.S Heaps Editor). American Geophysical Union, Washington, DC, 1-16.

Bretschneider, C. L., and R.O. Reid (1954) Changes in wave height due to bottom friction, percolation, and refraction. Tech. memo., Beach Erosion Board, U.S. Army Corps of Engineers, *45*, 36pp.

Burrows, M., and S.A. Thorpe (1999) Drifter observations of the Hebrides slope current and nearby circulation patterns. *Ann. Geophysicae*, 17, 280-302.

Garria, G., P. Lazure, B. Le Cann, A. Serpette, G. Reverdin, S. Louazel, F. Batioulier, F. Dumas, A. Pichon, and Y. Morel (2013) Surface layer circulation derived from Lagrangian drifters in the Bay of Biscay. *J. Mar. Systems*, 109-110, 60-76.

Egbert, G.D., and S.Y. Erofeeva (2002) Efficient inverse modeling of barotropic ocean tides, *J. Atmos. Oceanic Technol., 19(2)*, 183–204.

Hasselmann, K. and J.I. Collins (1968) Spectral dissipation of finite-depth gravity waves due to turbulent bottom friction. *J. Marine Res.*, *26*, 1-12.

Hill, A.E., B.M. Hickey, F.A. Shillington, P.T. Strub, K.H. Brink, E.D. Barton, and A.C. Thomas (1998) Eastern ocean boundaries: Coastal Segment (E). The Sea, 11, edited by A.R. Robinson and K.H. Brink, 29-67.

Huthnance, J.M.(1973) Tidal current asymmetries over the Norfolk sandbanks. *Estuar. Coastal Mar. Sci.*, *1*,89-99.

Huthnance, J.M.(1984) Slope current and “JEBAR”. *J. Phys. Oceanogr.*, *14*, 795-810.

Huthnance, J.M. (1986) The Rockall slope current and shelf-edge processes. *Proc. R. Soc. Edin.*, 88B, 83-101.

Huthnance, J.M., and Gould (1989) On the northeast Atlantic slope current in:*Poleward flows along eastern ocean boundaries*, Ed. S.J. Neshyba et al., *Coastal and Estuarine Studies*, *34*, 76-81.

Huthnance, J.M. (1995) Circulation, exchange and water masses at the ocean margin: the role of the physical processes at the shelf edge. *Progr. Oceanogr.*, 35, 353-431.

Huthnance, J.M., J.T. Holt, and S.L. Wakelin (2009) Deep ocean exchange with west-European shelf seas. *Ocean Sci.*, 5, 621-634.

Joyce, T.M. (1989) On the in situ “calibration” of shipboard ADCP. *J. Atm. Oceanic Technol.*, 6, 169-172.

Inall, M.E., T. P. Rippeth, and T. J. Sherwin (2000) Impact of non-linear waves on the dissipation of internal tidal energy at a shelf break. *J. Geophys. Res.*, 102, 5733-5752.

Li, S., and T. A. McClimans (2000) On the stability of barotropic prograde and retrograde jets along a bottom slope. *J. Geophys. Res.*, *105*, 8847-8855.

Loder, J.W. (1980) Topographic rectification of tidal currents on the sides of Georges Bank. *J. Phys. Oceanogr.*, *10*, 1399-1416.

Marshall, J., A. Adcroft, C. Hill, L. Perelman, and C. Heisey (1997) A finite-volume, incompressible Navier-Stokes model for studies of the ocean on the parallel computers, *J. Geophys. Res.*, 105(C4), 8687-8705.

Pacanowski, R.C., and S.G.H. Philander (1981) Parameterisation of vertical mixing in numerical models of Tropical Oceans. *J. Phys. Oceanogr.*, *11*, 1443-1451.

Pingree, R.D., and B. Le Cann (1989) Geltic and Armonian Slope and shelf residual currents. *Prog. Oceanogr.*,23, 303-338.

Porter, M., M.E. Inall, J.A.M. Green, J.H. Simpson, A.C. Dale, and P.I.Miller (2016) Drifter observations in the summer time Bay of Biscay slope current. *J. Mar. Sys.*, 157, 65-74.

Putnam, J.A., and J. W. Johnson (1949) The dissipation of wave energy by bottom friction. *Trans. Amer. Geophys. Un.*, 30, 67-74.

Souza, A.J., J.H. Simpson, M. Harikrishnan and J. Malarkey (2001), Flow structure and seasonality in the Hebridean slope current. *Oceanologica Acta*, *24*, 63-76.

Stashchuk, N., and V. Vlasenko (2005) Topographic generation of internal waves by nonlinear superposition of tidal harmonics *Deep Sea Res. I*, *52*, 605-620.

Stashchuk, N., and V. Vlasenko (2016) Bottom trapped internal waves over the Malin Sea continental slope *Deep Sea Res. I*, *In press*. Available at: http://dx.doi.org/10.1016/j.dsr.2016.11.007

Wakelin, S.L., J.T. Holt and R. Proctor (2009) The influence of initial conditions and open boundary conditions on shelf circulation in an3D ocean-shelf model of the North East Atlantic. *Ocean Dyn.*, 59, 67-81.

Warner, S.J., P. MacCready, J.N. Moum, and J.D. Nash (2013) Measurement of tidal form drag using seafloor pressure sensors. *J. Phys. Oceanogr.*, 43, 1150-1172.

White, M., and P. Bower (1997) The shelf -edge current north-west of Ireland. *Ann. Geophysicae*, 15, 1076-1083.

Xing, J., and A.M. Davies (2001) Non-linear effect of internal tides on the generation of the tidal mean flow at the Hebrides shelf edge. *Geophys. Res. Lett.*, *28*, 3939-3942.

Zimmerman, J.T.F. (1980) Vorticity transfer by tidal currents over irregular topography. *J. Mar. Res.*, *38*, 601-630.

Table: Zonal (A) and meridional (B) discharge of eight principal tidal harmonics used in the model setup. ϕ_a and ϕ_b are the tidal phases.

	M_2	S_2	N_2	K_2	K_1	O_1	P_1	Q_1
$A(m^2s^{-1})$	30	14	8.2	3.5	1.78	0.98	0.67	0.56
ϕ_a(degr)	143	127	75	102	170	0	39	18
$B(m^2s^{-1})$	25	3	7.18	2.79	3.11	1.32	1.09	0.9
ϕ_b(degr)	28	0	125	146	115	63	78.5	47.5

charac

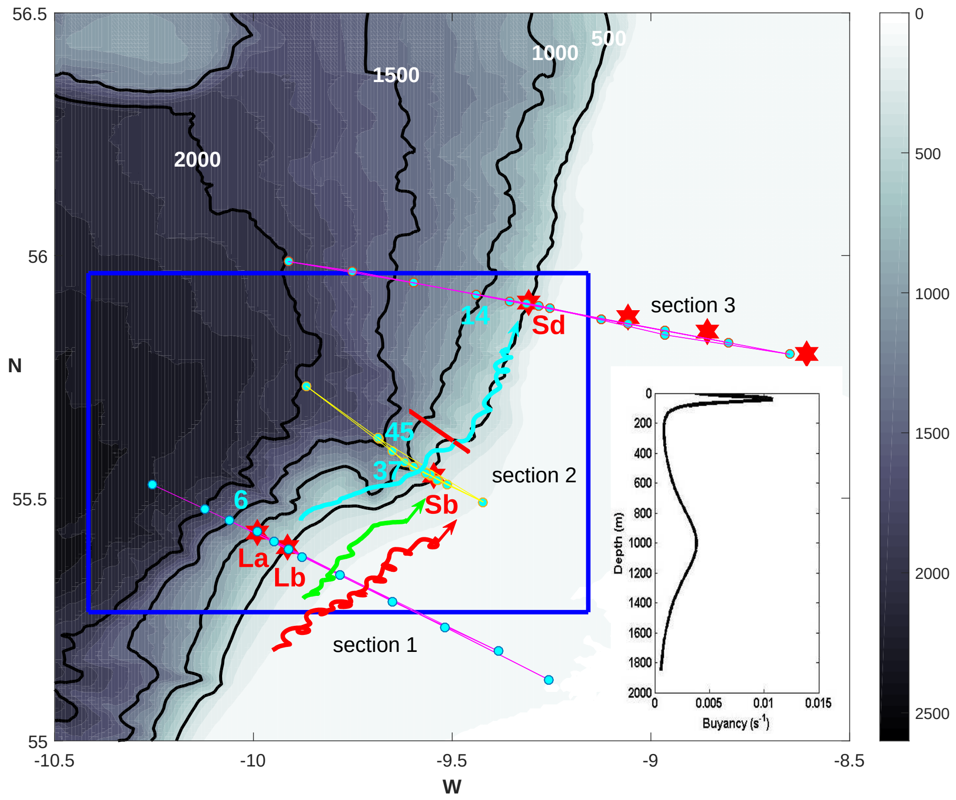

Figure 1: The bathymetry of the Malin Sea with the plan view of the JC88 field experiment. Cyan closed circle show positions of the CTD stations, red hexagrams depict the position of the moorings. Blue rectangle shows the model domain. An average buoyancy frequency profile is shown in the inset.

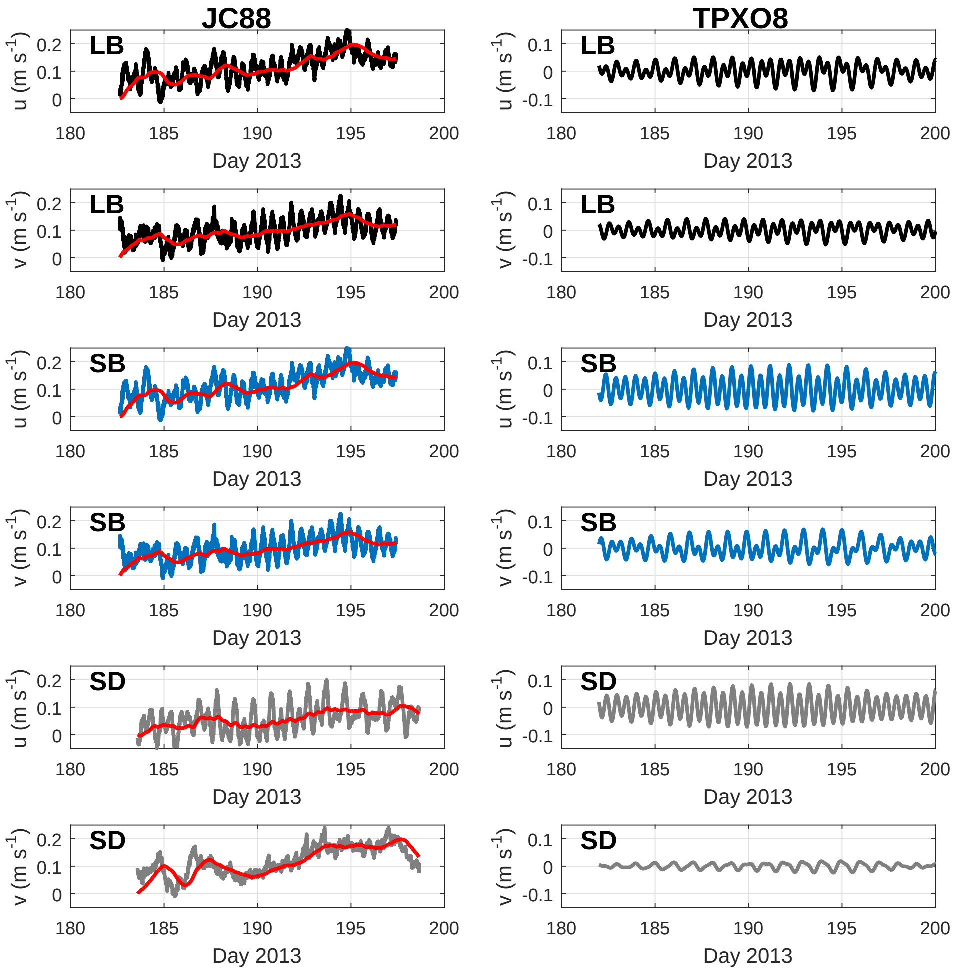

Figure 2: Zonal (u) and meridional (v) vertically averaged velocities recorded at moorings Lb, Sb, and Sd. Red lines show stationary currents. Left column: ADCP time series recorded during the JC88 cruise. Right column: TPXO8 predicted tidal currents.

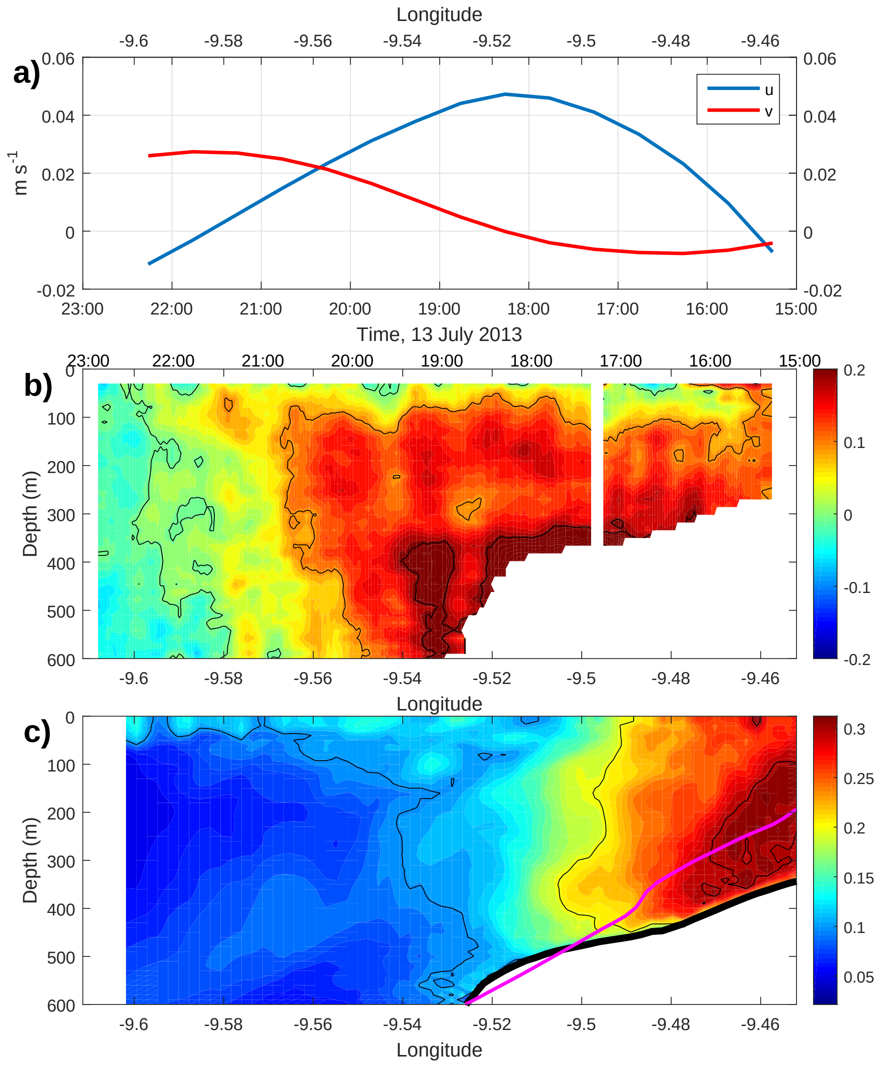

Figure 3: a) Zonal (u) and meridional (v) tidal currents predicted using TPXO8.1 tidal model for the time span (15.00-22.00) 13 July 2013 (bottom axis) at the positions across the slope shown by the upper axis. b) Along slope current recorded by a vessel mounted ADCP at the transect shown in Figure 1 by the red line. The time span of the transect is depicted at the top axis. c) Model predicted amplitudes of the along-slope horizontal velocities found for one tidal cycle. Magenta line depicts position of baroclinic tidal beam.

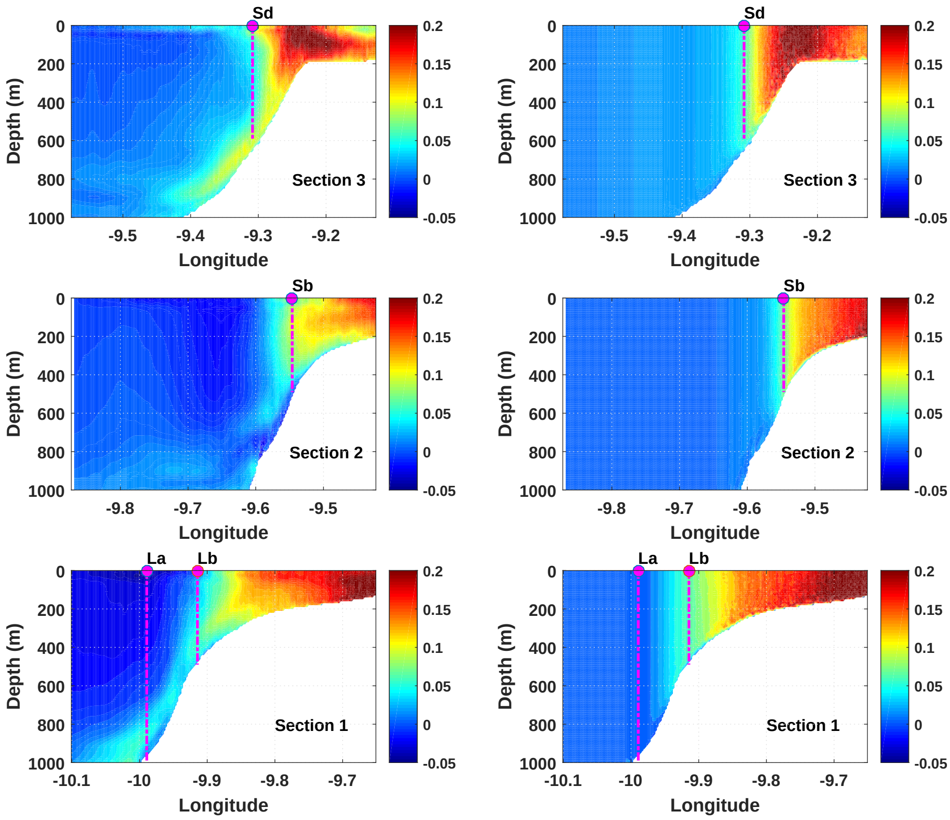

Figure 4: Model predicted along-slope residual current calculated by averaging of the model output over four days. Appropriate cross-sections with moorings Sd, Sb, La, Lb are shown in Figure 1. Left column stands for stratified fluid, the right column shows pure barotropic response.

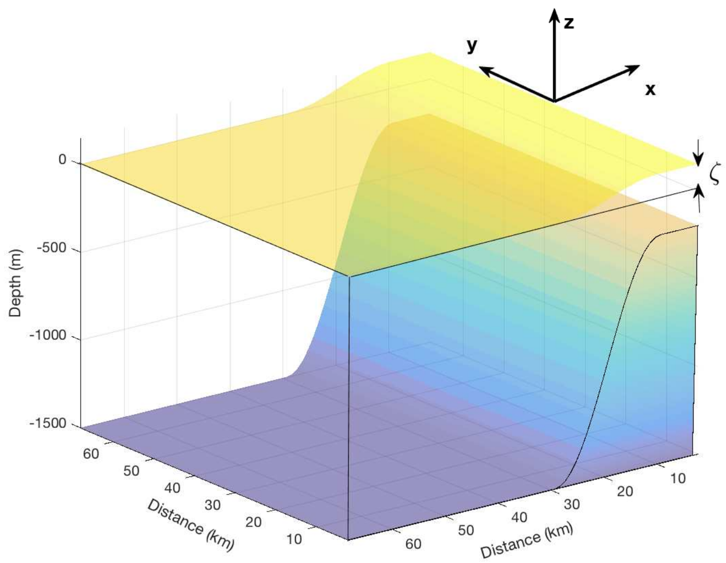

Figure 5: Schematic presentation of a two-dimensional slope-shelf topography oriented in south-north direction.

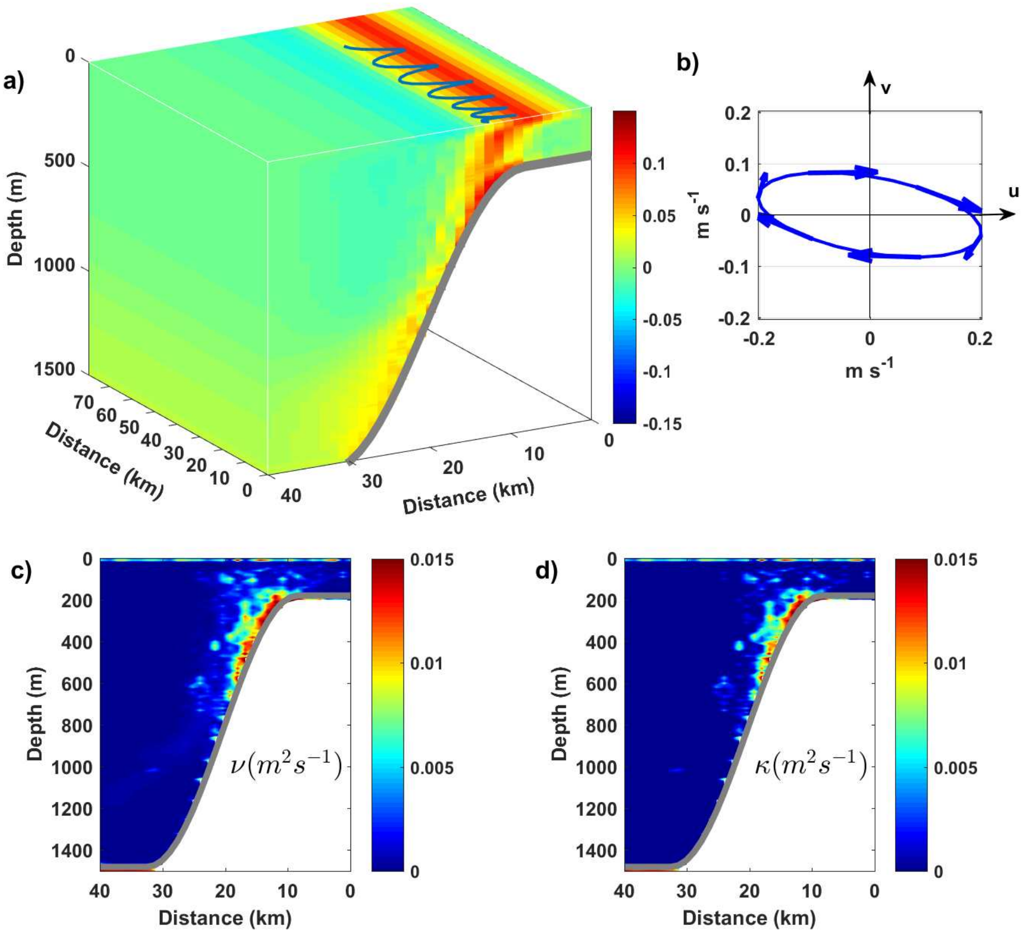

Figure 6: a) Spatial structure of the along-slope tidally induced rectified flow with the blue line showing a three-days trajectory of a passive tracer. b) Spatial structure and the scales of the tidal ellipse in the reference run. Panels c) and d) show spatial distributions of the viscosity ν and diffusivity κ coefficients set in the MITgcm by the KPP parameterization.

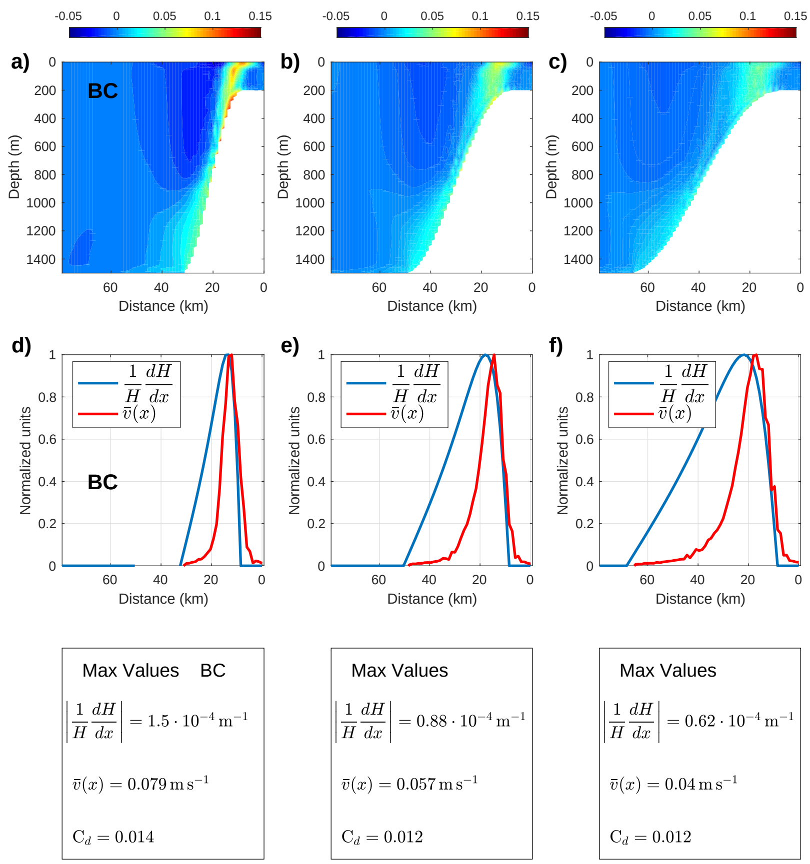

Figure 7: Panels a), b), c) illustrate spatial structure of the slope currents calculated for L =48, 84, and 120 km, respectively. Middle panels depict normalized depth integrated velocity (red) and the topographic term $\frac{1}{H}\frac{dH}{dx}$ (blue) for the same bottom profiles as above. Bottom panels show the maximum values of the parameters shown in panels d), e), and f).

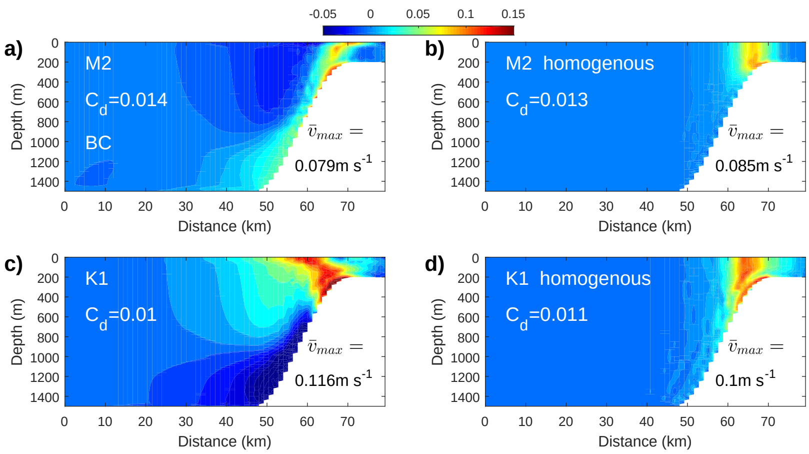

Figure 8: Spatial structure of residual currents induced by M_2 (panels a and b) and K_1 (panels c and d) tidal harmonics for the stratified (left column) and homogeneous (right column) fluids.

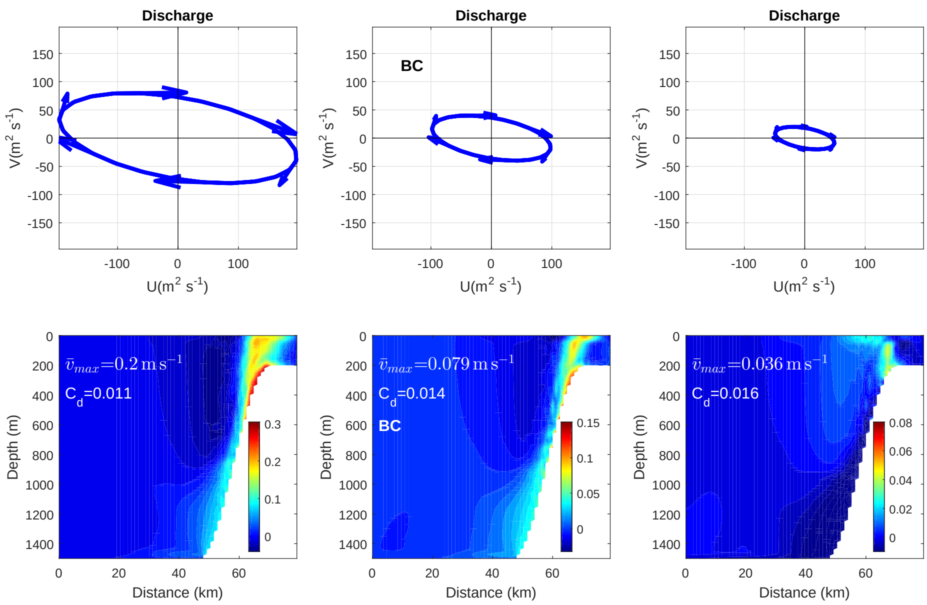

Figure 9: Residual currents induced by M_2 over 48 km wide continental slope in cases of strong, moderate, and weak tidal forcing (left, middle, and right columns, respectively). Appropriate tidal ellipses are shown in three top panels.

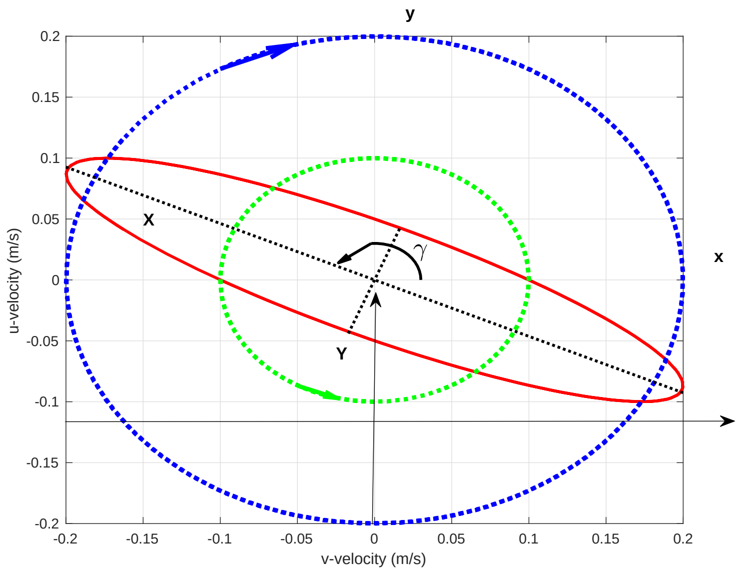

Figure 10: Tidal ellipse (red) presented as a superposition a clockwise (blue) and counter-clockwise (green) tidal velocity components. Angle γ shows the ellipse's inclination.

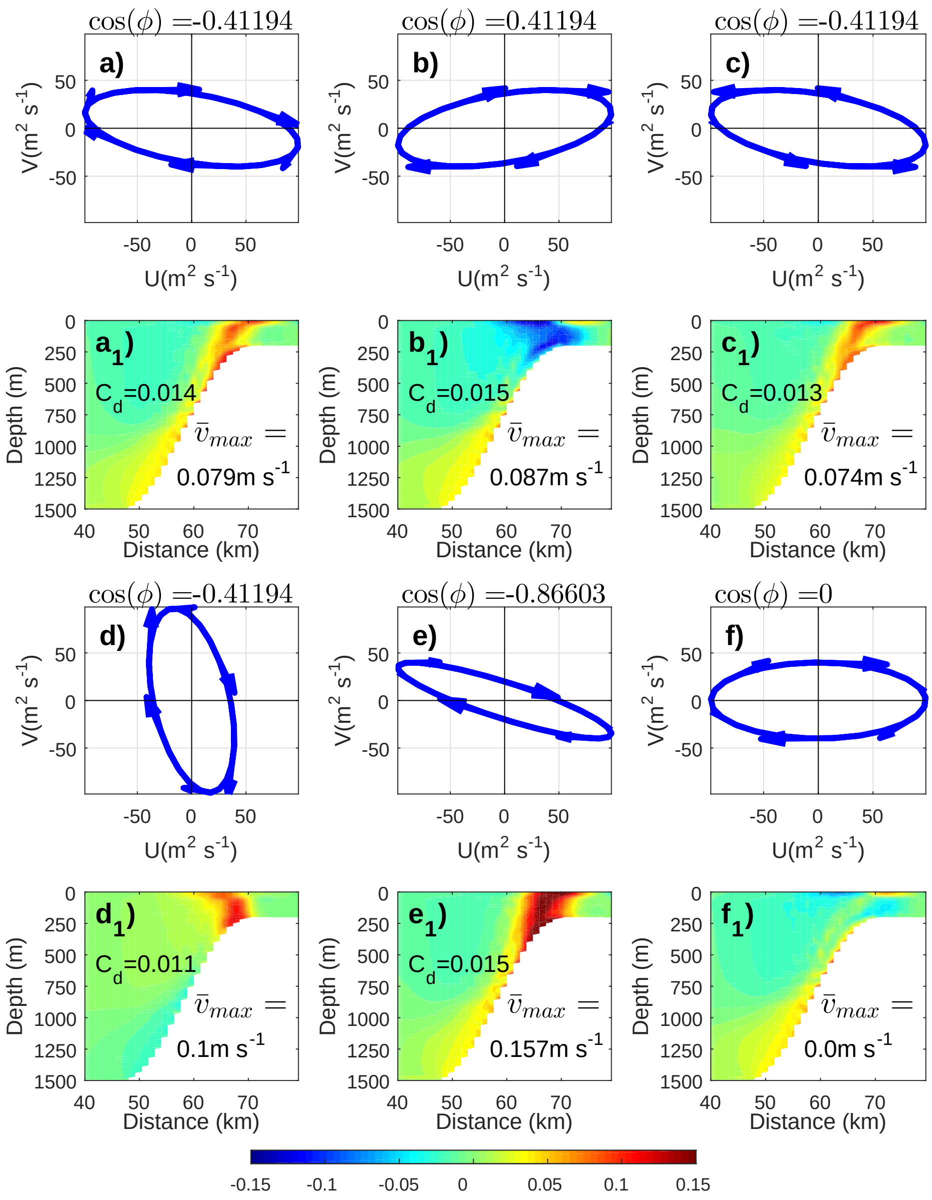

Figure 11: Influence of the tidal ellipses orientation (panels with blue ellipses) on the structure and strength of the along-slope rectified flow (shown in the second and fourth rows). Appropriate $\cos(\phi)$ value and maximum of the residual currents are depicted in the graphs.

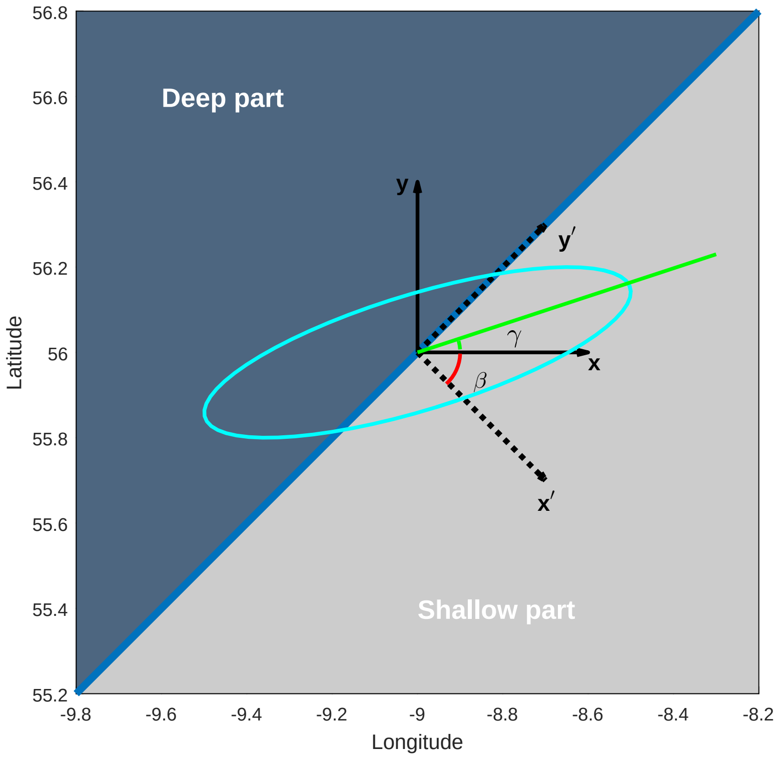

Figure 12: Schematic diagram showing the changes of the ellipse inclination angle γ after rotation of the co-ordinate system $(x0y)$ on the angle β that transforms it into system (x_r0y_r) with the axis $(0x)$ perpendicular to isobaths.

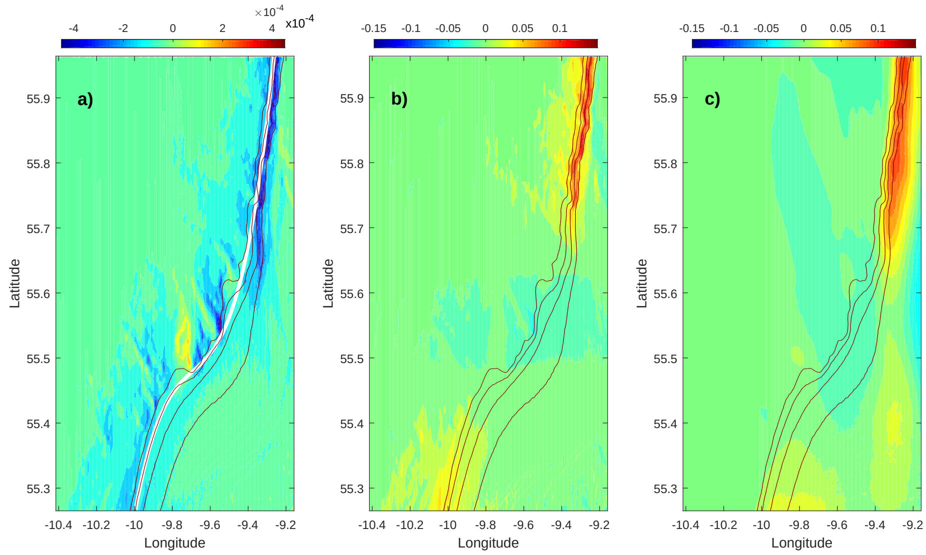

Figure 13: a) Bottom term $\frac{1}{H}\frac{\partial H}{\partial x}$. b) Rectified along-slope current v^c predicted by formula (7). c) Residual vertically average meridional current reproduced by the MITgcm for the Malin shelf/slope area.